NANO LETTERS

pubs.acs.org/NanoLett

Letter

# Controllable Thermal Conductivity in Twisted Homogeneous Interfaces of Graphene and Hexagonal Boron Nitride

Wengen Ouyang, Huasong Qin, Michael Urbakh,* and Oded Hod

Cite This: *Nano Lett.* 2020, 20, 7513−7518

Read Online

ACCESS | Metrics & More | Article Recommendations | Supporting Information

**ABSTRACT:** Thermal conductivity of homogeneous twisted stacks of graphite is found to strongly depend on the misfit angle. The underlying mechanism relies on the angle dependence of phonon−phonon couplings across the twisted interface. Excellent agreement between the calculated thermal conductivity of narrow graphitic stacks and corresponding experimental results indicates the validity of the predictions. This is attributed to the accuracy of interlayer interaction descriptions obtained by the dedicated registry-dependent interlayer potential used. Similar results for h-BN stacks indicate overall higher conductivity and reduced misfit angle variation. This opens the way for the design of tunable heterogeneous junctions with controllable heat-transport properties ranging from substrate-isolation to efficient heat evacuation.

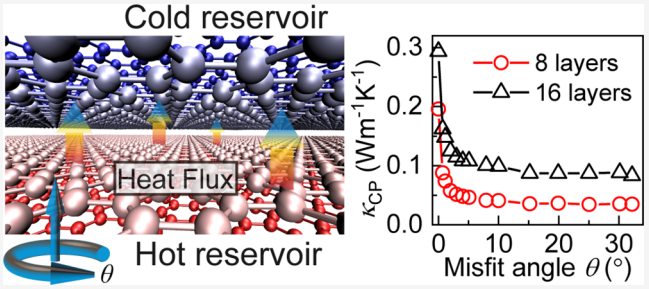


**KEYWORDS:** *Interfacial thermal conductivity, graphite, h-BN, twisted interface, misfit angle, phonon−phonon coupling, registry-dependent interlayer potential*



Graphene is considered to be one of the most promising heat dissipating materials in nanoelectronics[1−4] due to its ultrahigh in-plane room-temperature thermal conductivity of ∼3000−5000 W m$^{-1}$ K$^{-1}$.[5−7] This, however, can be hindered by graphene−substrate interactions that may lead to a substantial reduction of the heat-transport due to phonon leakage across the graphene−substrate interface and strong interfacial scattering of flexural phonon modes.[8] Such undesirable substrate effects can be reduced by considering multilayer graphene stacks. These are expected to effectively isolate the top graphene layers from the substrate due to the considerably lower cross-plane thermal conductivity (∼6.8 W m$^{-1}$ K$^{-1}$)[9] while exhibiting high in-plane conductivity that can be tuned via the stack thickness.[10−17] Anisotropic thermal conductivity is also observed for bulk hexagonal boron nitride (h-BN) with in-plane and cross-plane thermal conductivities in the range of 390−420 and 2.5−4.8 Wm$^{-1}$K$^{-1}$, respectively.[18,19]

Efficient in situ tuning of the thermal conductivity of such graphitic structures can be achieved by controlling the twist angle between adjacent layers within the stack. This has been recently computationally demonstrated for finite-sized nanoscale few-layer graphene junctions.[20,21] Two factors, however, limit the applicability of these results: (i) the simulations were performed using simplistic isotropic interlayer potentials that are known to be inaccurate for simulating the interlayer interactions in layered materials;[22−25] and (ii) the relevance of the results for large-scale interfaces is questionable due to significant edge scattering effects inherent to the small finite-sized model systems studied.

To address these issues, we use anisotropic potentials to investigate the interlayer thermal conductivity of periodic graphene and h-BN stacks of varying thicknesses and twist angles. This allows us to gain fundamental understanding of the heat transport mechanisms in layered materials stacks and identify feasible means to control it. Our model system consists of two contacting identical AB (AA′)-stacked graphite (h-BN) slabs, whose interfacing graphene (h-BN) layers are twisted with respect to each other to create a stacking fault of misfit angle $\theta$ (see Figure 1). Recent experiments demonstrated fine control over the misfit angle in such setups.[26,27] The thickness of the entire construction is varied between 2.7−35 nm (8−104 layers), and periodic boundary conditions are applied in all directions. Heat transport simulations are performed using state-of-the-art anisotropic interlayer potentials (ILP)[22−25] applied to the twisted stacks. These potentials were shown to capture well the structural, dynamic, and frictional properties of graphitic and h-BN layered systems, as well as their phonon spectra.[28−31] A thermal bias is induced by applying Langevin thermostats with different temperatures to two layers residing on opposite sides away from the twisted

**Received:** July 21, 2020
**Revised:** September 5, 2020
**Published:** September 8, 2020





https://dx.doi.org/10.1021/acs.nanolett.0c02983
*Nano Lett.* 2020, 20, 7513−7518

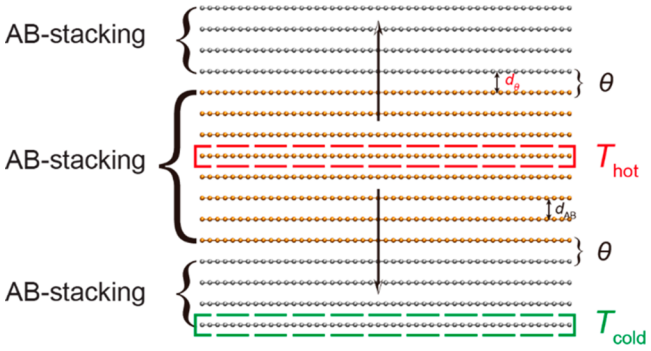


**Figure 1.** Schematic representation of the simulation setup. Two identical AB-stacked graphite slabs (gray and orange) are twisted with respect to each other to create a stacking fault of misfit angle $\theta$. A thermal bias is induced by applying Langevin thermostats to the two layers marked by dashed red ($T_{hot}$) and green ($T_{cold}$) rectangles. The arrows indicate the direction of the vertical heat flux. Since periodic boundary conditions are applied also in the vertical direction, two twisted interfaces are shown across which heat flows in opposite directions.

interface (see Sections 1 and 2 of the Supporting Information for further details).

We start by studying the effect of the misfit angle on the cross-plane thermal conductivity of the twisted graphite and h-BN stacks. Figure 2 presents the dependence of the cross-plane

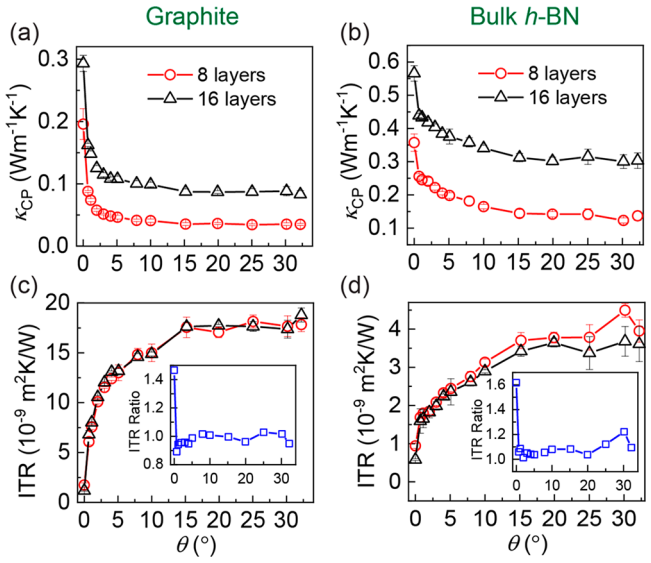


**Figure 2.** Twist-angle dependence of the cross-plane thermal conductivity of the entire stack (a,b), and the interfacial thermal resistance (c,d) of the twisted contact formed between the optimally stacked slabs of graphite (a,c) and bulk h-BN (b,d), respectively. Red circles and black triangles correspond to the results obtained using 8 and 16 layer models, respectively. The insets in panels c and d show the ratio between the twist angle-dependent ITR results obtained using 8 and 16 layer models. Error bars estimation procedure is discussed in Section 1 of the Supporting Information.

thermal conductivity of the entire stack on the misfit angle for model systems consisting of 8 (red circles) and 16 (black triangles) layers for (a) graphite and (b) h-BN. A pronounced dependence of the cross-plane thermal conductivity ($\kappa_{CP}$) of the entire graphitic stack is clearly evident, which above a misfit angle of ∼5° drops by a factor of 3−4 with respect to the value obtained for the aligned contact. Similar misfit-angle dependence of $\kappa_{CP}$ is obtained for twisted bilayer graphene (tBLG) using the transient MD simulation approach (see Section 4 of Supporting Information). We note that this sharp drop for graphite is steeper and that the overall reduction is higher than those previously obtained using Lennard-Jones (LJ) interlayer potentials in finite model systems.[20,21] The corresponding cross-plane thermal conductivity of the commensurate h-BN stack is found to be approximately double that of graphite for the same number of layers. Notably, it reduces more gradually with the twist angle and saturates at ∼15° with an overall 2−3-fold reduction.

The thermal conductivity of both graphite and h-BN stacks is found to increase when doubling their thickness. To identify the source of this thickness dependence we plot in Figure 2c,d the interfacial thermal resistance (ITR) (see Section 1.2 of Supporting Information for the definition) associated with the twisted junction formed between the contacting graphene or h-BN layers of the two optimally stacked slabs. Note that unlike $\kappa_{CP}$, which measures the conductivity of the entire stack, the ITR corresponds to the heat transport resistance of the two adjacent layers forming the twisted interface. Two important observations can be made: (i) The ITR, which measures only the resistance of the twisted interface, weakly depends on the slab thickness for any twist angle larger than zero (see insets of Figure 2c,d) indicating that the thickness dependence mainly arises from the conductivity of the optimally stacked slabs residing above and below the interface. Specifically, in the thickness range considered, the thinner the sample, the smaller the number of phonon modes that contribute to the thermal conductivity. This is because phonons of wavelength larger than the system thickness are eliminated. This reduction in density of vertical heat carrying phonon modes results in a decrease of the overall thermal conductivity with decreasing thickness.[32−34] (ii) The ITR strongly depends on the twist angle demonstrating a ∼10-fold (4-fold) increase when the twist angle at the graphene (h-BN) interface is varied from 0° to 15°. This clearly indicates that the twist angle can be utilized to control the cross-plane thermal conductivity of hexagonal two-dimensional (2D) materials and to effectively thermally isolate the top layers from the underlying substrate.

The strong dependence of the cross-plane thermal conductivity of graphene and h-BN on the stacking fault twist angle is related to the degree of coupling between the phonon modes of the two contacting layers at the twisted interface. Note that the term "coupling" used herein is not related to the standard notion of phonon−phonon couplings due to anharmonic effects. Instead, we regard to the off-diagonal terms of the Hessian when represented in the basis of the harmonic phonon modes of the isolated layers. To demonstrate this, we write the dynamical matrix (the mass-reduced Fourier transform of the force constant matrix) in block form as follows

$$\mathbf{\Phi}(\mathbf{q}) = \begin{pmatrix} \mathbf{\Phi}_{11}(\mathbf{q}) & \mathbf{\Phi}_{12}(\mathbf{q}) \\ \mathbf{\Phi}_{21}(\mathbf{q}) & \mathbf{\Phi}_{22}(\mathbf{q}) \end{pmatrix} \quad (1)$$

where $\mathbf{\Phi}_{11}(\mathbf{q})$ and $\mathbf{\Phi}_{22}(\mathbf{q})$ are the block matrices relating to the first and second layer and $\mathbf{\Phi}_{12}(\mathbf{q})$ and $\mathbf{\Phi}_{21}(\mathbf{q}) = \mathbf{\Phi}_{12}^{\dagger}(\mathbf{q})$, all evaluated at wavevector $\mathbf{q}$. The interlayer phonon−phonon couplings are obtained by diagonalizing separately $\mathbf{\Phi}_{11}(\mathbf{q})$ and $\mathbf{\Phi}_{22}(\mathbf{q})$ such that $\tilde{\mathbf{\Phi}}_{11}(\mathbf{q}) = \boldsymbol{U}_1^{\dagger}(\mathbf{q})\mathbf{\Phi}_{11}(\mathbf{q})\boldsymbol{U}_1(\mathbf{q})$ and $\tilde{\mathbf{\Phi}}_{22}(\mathbf{q}) = \boldsymbol{U}_2^{\dagger}(\mathbf{q})\mathbf{\Phi}_{22}(\mathbf{q})\boldsymbol{U}_2(\mathbf{q})$ are diagonal matrices containing the


https://dx.doi.org/10.1021/acs.nanolett.0c02983
Nano Lett. 2020, 20, 7513−7518

frequencies ($\omega_i$) of the phonon modes of the two layers and $\boldsymbol{U}_1(\mathbf{q})$ and $\boldsymbol{U}_2(\mathbf{q})$ are unitary matrices of the corresponding eigenvectors. We now construct a global block diagonal transformation matrix of the form

$$\boldsymbol{U}(\mathbf{q}) = \begin{pmatrix} \boldsymbol{U}_1(\mathbf{q}) & \mathbf{0} \\ \mathbf{0} & \boldsymbol{U}_2(\mathbf{q}) \end{pmatrix} \tag{2}$$

and transform the full dynamical matrix as follows

$$\boldsymbol{U}^{\dagger}(\mathbf{q})\boldsymbol{\Phi}(\mathbf{q})\boldsymbol{U}(\mathbf{q}) = \begin{pmatrix} \tilde{\boldsymbol{\Phi}}_{11}(\mathbf{q}) & \tilde{\boldsymbol{\Phi}}_{12}(\mathbf{q}) \\ \tilde{\boldsymbol{\Phi}}_{21}(\mathbf{q}) & \tilde{\boldsymbol{\Phi}}_{22}(\mathbf{q}) \end{pmatrix} \tag{3}$$

where $\tilde{\boldsymbol{\Phi}}_{12}(\mathbf{q}) = \boldsymbol{U}_1^{\dagger}(\mathbf{q})\boldsymbol{\Phi}_{12}(\mathbf{q})\boldsymbol{U}_2(\mathbf{q})$ and $\tilde{\boldsymbol{\Phi}}_{21}(\mathbf{q}) = \tilde{\boldsymbol{\Phi}}_{12}^{\dagger}(\mathbf{q})$ are the interlayer phonon−phonon coupling blocks. Naturally, when the two layers are infinitely separated, these coupling blocks vanish and the diagonal blocks converge to those of the isolated layers.

The overall coupling between the two layers can be obtained from the individual phonon−phonon coupling matrix elements via Fermi's golden rule,[35] which reads as (see Section 7 of the Supporting Information for a detailed derivation):

$$\Gamma_{\text{tot}} = \frac{\pi\hbar^3}{2}\sum_{\mathbf{q}\lambda}\frac{e^{-\beta E_{\mathbf{q}\lambda}}}{Z}\frac{\rho(E_{\mathbf{q}\lambda})|V_{\lambda,\lambda+3r/2}(\mathbf{q})|^2}{E_{\mathbf{q}\lambda}^2} \tag{4}$$

where $Z = \sum_{\mathbf{q}\lambda} e^{-\beta E_{\mathbf{q}\lambda}}$ is the partition function, $E_{\mathbf{q}\lambda}$ is the energy of phonons at branch $\lambda$ with wavevector $\mathbf{q}$, $\rho(E_{\mathbf{q}\lambda})$ is the density of states (DOS) at $E_{\mathbf{q}\lambda}$, and $|V_{\lambda,\lambda+3r/2}(\mathbf{q})|^2$ is the coupling matrix element between branches of phonons of similar energy in the two layers, whose number of atoms in one unit cell is $r$. Note that Fermi's golden rule derived in Section 7 of the Supporting Information and presented in eq 4 is closely related to the equivalent electronic transport expression derived from the Landauer−Büttiker approach[36,37] within the nonequilibrium Green's function formalism.[38,39]

Using eq 4, we can rationalize the misfit angle dependence of the heat flux across the twisted interface from the calculated interphonon coupling. To that end, we performed room-temperature (300 K) simulations (technical details can be found in Section 5 of the Supporting Information) for tBLG with different misfit angles using the Green's function molecular dynamics (GFMD) approach developed by Kong et al.[40] as implemented in LAMMPS.[41] The simulations allow us to evaluate the dynamical matrix from which the phonon−phonon couplings can be extracted (see details in Section 5 of the Supporting Information) and the overall heat transfer rate calculated. Figure 3 shows the resulting heat transfer rate (normalized to the value obtained for the aligned contact ($\theta$ = 0)) as a function of the misfit angle compared to the interfacial thermal conductivity (ITC) defined as the inverse of the ITR presented in Figure 2c, ITC ≡ 1/ITR. The agreement between the calculated ITC and the Fermi's golden rule results indicates that the dependence of the interlayer phonon−phonon couplings on the misfit angle is responsible for the strong angle dependence of the interfacial conductivity. Notably, the sharp heat conductivity drop at misfit angles in the range of 0°−5° as well as the small conductivity for larger misfit angles are well captured by Fermi's golden rule.

To correlate our results with experimentally measured thermal conductivities that are often obtained for thick samples, we repeated our calculations for increasing stack

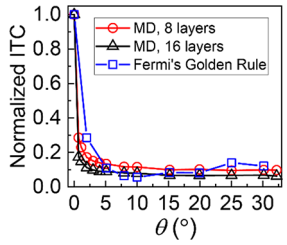


**Figure 3.** Comparison between Fermi's golden rule results (open blue squares) for the interfacial heat-transfer rate of a tBLG and the calculated interfacial thermal conductivity at various misfit angles. ITC simulation results are presented for both 8 layers (open red circles) and 16 layers (open black triangles) showing similar behavior. For comparison purposes, all data sets are normalized to their value obtained for the aligned contact.

thicknesses at fixed misfit angles. Figure 4 presents results for the calculated heat conductivity of graphite (panel a) and h-BN (panel b) stacks either aligned (open red circles) or twisted by $\theta$ = 30.16° (open black diamond symbols) as a function of the number of layers in the stack. As discussed above, for both systems the misoriented stack exhibits lower heat conductivity compared to the aligned system, however, its thickness dependence is considerably stronger. This can be attributed to the significantly higher interface resistance of the twisted interface (see Figure 4c,d) that when plugged in eq S1.2 of Section 1.3 in the Supporting Information for the overall conductivity induces stronger thickness dependence (see Section 4.2 of the Supporting Information).

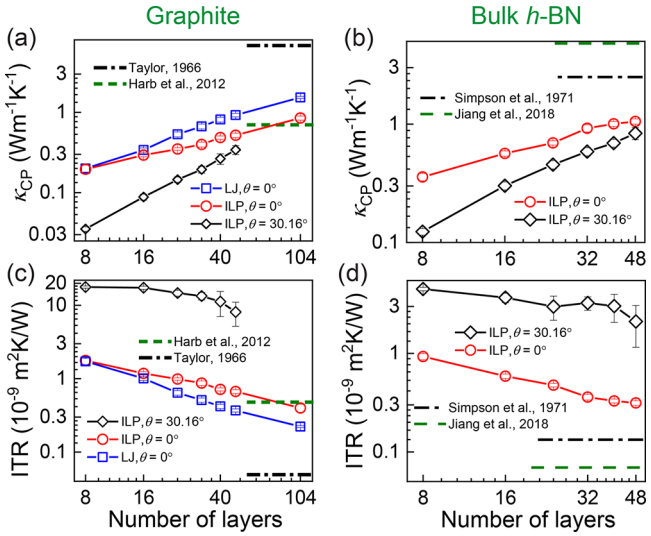


**Figure 4.** Thickness dependence of the thermal conductivity, $\kappa_{CP}$, of aligned (open red circles) and twisted by 30.16° (open black diamond symbols) graphite (a) and h-BN (b) stacks. Blue squares represent results obtained using the isotropic Lennard-Jones potential for the aligned contacts. The green dashed and black dash-dotted lines represent experimental results measured for graphite (a) (refs 9 and 42) and bulk h-BN (b) (refs 18 and 19). Panels (c) and (d) show the thickness dependence of the ITR extracted, using eq S1.2 in Section 1.3 of the Supporting Information, from the $\kappa_{CP}$ results for the graphitic and h-BN junctions as presented in panels (a) and (b), respectively, using the same color code. Note that both axis scales are logarithmic. Error bars estimation procedure is discussed in Section 1 of the Supporting Information.



https://dx.doi.org/10.1021/acs.nanolett.0c02983
Nano Lett. 2020, 20, 7513−7518

Comparing our calculated heat conductivities for the aligned contact (open red circles) to available experimental data for ~35 nm thick graphite slabs[42] (dashed green line), we find that at the thickest model system considered of 104 graphene layers (~35.4 nm thick) the calculated value of 0.85 ± 0.05 W/m·K is in agreement with the measured value of ~0.7 W/m·K. Furthermore, experimental values for bulk graphite[9] indicate that the thermal conductivity continues to grow up to ~6.8 W/m·K (black dash-dotted line), which is consistent with the general trend of the calculated heat conductivity that does not saturate for the thickest model system considered. These results support the validity of our force-field and model systems to study the heat conductivity of twisted layered material interfaces. Available experimental results for the heat conductivity of bulk h-BN are marked by the dashed-dotted black and dashed-green lines in Figure 4b. In line with our findings for the graphitic interface, our calculated finite slab heat conductivities for the aligned interface (open red circles) continue to grow with the number of layers and are consistently below the bulk value.

Another important factor that may affect the interlayer thermal transport properties of 2D material stacks is the average temperature of the system, which was taken to be ~300 K in all above-mentioned simulations. To evaluate the sensitivity of our results toward this parameter, we repeated the heat conductivity and interfacial resistance calculations of optimally stacked graphite and h-BN stacks for an average temperature of 400 K. The results, presented in Section 6 of the Supporting Information, indicate that the thickness dependence of $\kappa_{CP}$ exhibits qualitatively similar behavior also at an average temperature of 400 K with a nearly uniform decrease in magnitude.

We note that previous calculations of the heat conductivity of twisted graphitic interfaces relied on LJ potentials describing the interlayer interactions.[12−14,17] To demonstrate the effect of using registry-dependent interlayer potentials, we have repeated our calculations of the heat conductivity of graphitic slabs with the REBO intralayer potential augmented by LJ interlayer interactions[43] ($\varepsilon$ = 2.84 meV, $\sigma$ = 3.4 Å). We find that the calculated heat conductivities obtained using the LJ interlayer potential are consistently higher than those obtained by our ILP and that the difference between them grows with the model system thickness. Notably, the heat conductivity obtained using the LJ potential for a graphitic slab of thickness ~35.4 nm is 1.54 W/m·K, overestimating the experimental value by more than a factor of 2. However, it should be noted that the absolute value of the thermal conductivity might be quite sensitive to the simulation protocol used[44] (see Section 4 of the Supporting Information), thus close attention should be paid when calculating it for nanoscale structures from MD simulations (see details in Section 2 of the Supporting Information).

The agreement between our ILP calculations of the thermal conductivity and phonon spectrum of nanoscale graphitic stacks (see Section 3 of the Supporting Information) with the corresponding experimental data, therefore, demonstrates the reliability of our predictions for the strong interfacial misfit angle dependence of cross-layer thermal conductivity in graphite and h-BN. The observed sharp conductivity decrease of twisted graphitic interfaces at misfit angles <5° opens the way to control the thermal evacuation rate and thermal isolation of active layers in graphene-based electronic and mechanical devices. The revealed underlying mechanism suggests that design rules can be obtained by carefully tailoring the phonon−phonon couplings across the twisted interface. While the misfit angle dependence of h-BN is found to be weaker than that of graphite, the overall thermal conductivity of the former is found to be higher. This may be utilized to achieve higher conductivity and controllability in twisted heterogeneous junctions of layered materials.

Finally, we note that quantum effects[45,46] on thermal transport properties are not considered within our classical MD simulations. However, it should be noted that the contribution of such effects to the calculated thermal conductivity was found to be important only below the Debye temperature.[47,48] For instance, two recent studies found that the quantum corrected in-plane thermal conductivity of graphene nanoribbons is close to the value obtained by classical MD simulations above the Debye temperature of 322 K.[49,50] In the case of cross-plane thermal conductivity, the relevant Debye temperature is 180.5 K,[9] well below the temperatures used in our simulations. Therefore, we expect quantum corrections to have a minor effect on the quantitative nature of our results and a negligible effect on the qualitative conclusions.

## ■ ASSOCIATED CONTENT

### Supporting Information

The Supporting Information is available free of charge at https://pubs.acs.org/doi/10.1021/acs.nanolett.0c02983.

Methodology; convergece tests; comparison of the phonon spectrum and density of states calculated using the ILP and the Lennard-Jones potential; thermal conductivity of twisted bilayer graphene; theory for calculating the phonon coupling of twisted bilayer graphene; temperature dependence of the cross-plane thermal conductivity, and derivation of Fermi's golden rule (PDF)

## ■ AUTHOR INFORMATION


### Corresponding Author

**Michael Urbakh** − *Department of Physical Chemistry, School of Chemistry, The Raymond and Beverly Sackler Faculty of Exact Sciences and The Sackler Center for Computational Molecular and Materials Science, Tel Aviv University, Tel Aviv 6997801, Israel;* orcid.org/0000-0002-3959-5414; Email: urbakh@tauex.tau.ac.il

### Authors

**Wengen Ouyang** − *Department of Physical Chemistry, School of Chemistry, The Raymond and Beverly Sackler Faculty of Exact Sciences and The Sackler Center for Computational Molecular and Materials Science, Tel Aviv University, Tel Aviv 6997801, Israel;* orcid.org/0000-0001-8700-1978

**Huasong Qin** − *State Key Laboratory for Strength and Vibration of Mechanical Structures, School of Aerospace, Xi'an Jiaotong University, Xi'an 710049, China*

**Oded Hod** − *Department of Physical Chemistry, School of Chemistry, The Raymond and Beverly Sackler Faculty of Exact Sciences and The Sackler Center for Computational Molecular and Materials Science, Tel Aviv University, Tel Aviv 6997801, Israel;* orcid.org/0000-0003-3790-8613

Complete contact information is available at: https://pubs.acs.org/10.1021/acs.nanolett.0c02983




https://dx.doi.org/10.1021/acs.nanolett.0c02983
Nano Lett. 2020, 20, 7513−7518

## Notes

The authors declare no competing financial interest.

## ■ ACKNOWLEDGMENTS

The authors would like to thank Prof. Abraham Nitzan, Dr. Guy Cohen, and Dr. Yiming Pan for helpful discussions. W.O. acknowledges the financial support of the fellowship program for outstanding postdoctoral researchers from China and India in Israeli Universities and the support from the National Natural Science Foundation of China (Nos. 11890673 and 11890674). H.Q. acknowledges the financial support from the National Natural Science Foundation of China (No. 11890674). M.U. acknowledges the financial support of the Israel Science Foundation, Grant 1141/18 and the ISF-NSFC joint Grant 3191/19. O.H. is grateful for the generous financial support of the Israel Science Foundation under Grant 1586/17 and the Naomi Foundation for generous financial support via the 2017 Kadar Award. This work is supported in part by COST Action MP1303.

## ■ REFERENCES

(1) Balandin, A. A. Thermal properties of graphene and nanostructured carbon materials. *Nat. Mater.* **2011**, *10* (8), 569−581.
(2) Li, N.; Ren, J.; Wang, L.; Zhang, G.; Hänggi, P.; Li, B. Colloquium: Phononics: Manipulating heat flow with electronic analogs and beyond. *Rev. Mod. Phys.* **2012**, *84* (3), 1045−1066.
(3) Xu, Z. Heat transport in low-dimensional materials: A review and perspective. *Theor. Appl. Mech. Lett.* **2016**, *6* (3), 113−121.
(4) Nika, D. L.; Balandin, A. A. Phonons and thermal transport in graphene and graphene-based materials. *Rep. Prog. Phys.* **2017**, *80* (3), No. 036502.
(5) Ghosh, S.; Calizo, I.; Teweldebrhan, D.; Pokatilov, E. P.; Nika, D. L.; Balandin, A. A.; Bao, W.; Miao, F.; Lau, C. N. Extremely high thermal conductivity of graphene: Prospects for thermal management applications in nanoelectronic circuits. *Appl. Phys. Lett.* **2008**, *92* (15), 151911.
(6) Balandin, A. A.; Ghosh, S.; Bao, W.; Calizo, I.; Teweldebrhan, D.; Miao, F.; Lau, C. N. Superior thermal conductivity of single-layer graphene. *Nano Lett.* **2008**, *8* (3), 902−907.
(7) Xu, X.; Pereira, L. F. C.; Wang, Y.; Wu, J.; Zhang, K.; Zhao, X.; Bae, S.; Tinh Bui, C.; Xie, R.; Thong, J. T. L.; Hong, B. H.; Loh, K. P.; Donadio, D.; Li, B.; Özyilmaz, B. Length-dependent thermal conductivity in suspended single-layer graphene. *Nat. Commun.* **2014**, *5* (1), 3689.
(8) Seol, J. H.; Jo, I.; Moore, A. L.; Lindsay, L.; Aitken, Z. H.; Pettes, M. T.; Li, X.; Yao, Z.; Huang, R.; Broido, D.; Mingo, N.; Ruoff, R. S.; Shi, L. Two-Dimensional Phonon Transport in Supported Graphene. *Science* **2010**, *328* (5975), 213−216.
(9) Taylor, R. The thermal conductivity of pyrolytic graphite. *Philos. Mag.* **1966**, *13* (121), 157−166.
(10) Ghosh, S.; Bao, W.; Nika, D. L.; Subrina, S.; Pokatilov, E. P.; Lau, C. N.; Balandin, A. A. Dimensional crossover of thermal transport in few-layer graphene. *Nat. Mater.* **2010**, *9*, 555.
(11) Wang, Z.; Xie, R.; Bui, C. T.; Liu, D.; Ni, X.; Li, B.; Thong, J. T. L. Thermal Transport in Suspended and Supported Few-Layer Graphene. *Nano Lett.* **2011**, *11* (1), 113−118.
(12) Wei, Z.; Ni, Z.; Bi, K.; Chen, M.; Chen, Y. Interfacial thermal resistance in multilayer graphene structures. *Phys. Lett. A* **2011**, *375* (8), 1195−1199.
(13) Ni, Y.; Chalopin, Y.; Volz, S. Significant thickness dependence of the thermal resistance between few-layer graphenes. *Appl. Phys. Lett.* **2013**, *103* (6), No. 061906.
(14) Chen, J.; Walther, J. H.; Koumoutsakos, P. Strain Engineering of Kapitza Resistance in Few-Layer Graphene. *Nano Lett.* **2014**, *14* (2), 819−825.
(15) Fu, Q.; Yang, J.; Chen, Y.; Li, D.; Xu, D. Experimental evidence of very long intrinsic phonon mean free path along the c-axis of graphite. *Appl. Phys. Lett.* **2015**, *106* (3), No. 031905.
(16) Fugallo, G.; Cepellotti, A.; Paulatto, L.; Lazzeri, M.; Marzari, N.; Mauri, F. Thermal Conductivity of Graphene and Graphite: Collective Excitations and Mean Free Paths. *Nano Lett.* **2014**, *14* (11), 6109−6114.
(17) Wei, Z.; Yang, J.; Chen, W.; Bi, K.; Li, D.; Chen, Y. Phonon mean free path of graphite along the c-axis. *Appl. Phys. Lett.* **2014**, *104* (8), No. 081903.
(18) Sichel, E. K.; Miller, R. E.; Abrahams, M. S.; Buiocchi, C. J. Heat capacity and thermal conductivity of hexagonal pyrolytic boron nitride. *Phys. Rev. B* **1976**, *13* (10), 4607−4611.
(19) Jiang, P.; Qian, X.; Yang, R.; Lindsay, L. Anisotropic thermal transport in bulk hexagonal boron nitride. *Phys. Rev. Mater.* **2018**, *2* (6), No. 064005.
(20) Wang, M.-H.; Xie, Y.-E.; Chen, Y.-P. Thermal transport in twisted few-layer graphene. *Chin. Phys. B* **2017**, *26* (11), 116503.
(21) Nie, X.; Zhao, L.; Deng, S.; Zhang, Y.; Du, Z. How interlayer twist angles affect in-plane and cross-plane thermal conduction of multilayer graphene: A non-equilibrium molecular dynamics study. *Int. J. Heat Mass Transfer* **2019**, *137*, 161−173.
(22) Kolmogorov, A. N.; Crespi, V. H. Registry-dependent interlayer potential for graphitic systems. *Phys. Rev. B: Condens. Matter Mater. Phys.* **2005**, *71* (23), 235415.
(23) Reguzzoni, M.; Fasolino, A.; Molinari, E.; Righi, M. C. Potential energy surface for graphene on graphene: Ab initio derivation, analytical description, and microscopic interpretation. *Phys. Rev. B: Condens. Matter Mater. Phys.* **2012**, *86* (24), 245434.
(24) van Wijk, M. M.; Schuring, A.; Katsnelson, M. I.; Fasolino, A. Moire' Patterns as a Probe of Interplanar Interactions for Graphene on h-BN. *Phys. Rev. Lett.* **2014**, *113* (13), 135504.
(25) Mandelli, D.; Ouyang, W.; Urbakh, M.; Hod, O. The Princess and the Nanoscale Pea: Long-Range Penetration of Surface Distortions into Layered Materials Stacks. *ACS Nano* **2019**, *13* (7), 7603−7609.
(26) Koren, E.; Lörtscher, E.; Rawlings, C.; Knoll, A. W.; Duerig, U. Adhesion and friction in mesoscopic graphite contacts. *Science* **2015**, *348* (6235), 679−683.
(27) Koren, E.; Leven, I.; Lörtscher, E.; Knoll, A.; Hod, O.; Duerig, U. Coherent commensurate electronic states at the interface between misoriented graphene layers. *Nat. Nanotechnol.* **2016**, *11*, 752.
(28) Ouyang, W.; Azuri, I.; Mandelli, D.; Tkatchenko, A.; Kronik, L.; Urbakh, M.; Hod, O. Mechanical and Tribological Properties of Layered Materials under High Pressure: Assessing the Importance of Many-Body Dispersion Effects. *J. Chem. Theory Comput.* **2020**, *16* (1), 666−676.
(29) Ouyang, W.; Mandelli, D.; Urbakh, M.; Hod, O. Nanoserpents: Graphene Nanoribbon Motion on Two-Dimensional Hexagonal Materials. *Nano Lett.* **2018**, *18* (9), 6009−6016.
(30) Leven, I.; Maaravi, T.; Azuri, I.; Kronik, L.; Hod, O. Interlayer Potential for Graphene/h-BN Heterostructures. *J. Chem. Theory Comput.* **2016**, *12* (6), 2896−905.
(31) Maaravi, T.; Leven, I.; Azuri, I.; Kronik, L.; Hod, O. Interlayer Potential for Homogeneous Graphene and Hexagonal Boron Nitride Systems: Reparametrization for Many-Body Dispersion Effects. *J. Phys. Chem. C* **2017**, *121* (41), 22826−22835.
(32) Liang, L. H.; Li, B. Size-dependent thermal conductivity of nanoscale semiconducting systems. *Phys. Rev. B: Condens. Matter Mater. Phys.* **2006**, *73* (15), 153303.
(33) Schelling, P. K.; Phillpot, S. R.; Keblinski, P. Comparison of atomic-level simulation methods for computing thermal conductivity. *Phys. Rev. B: Condens. Matter Mater. Phys.* **2002**, *65* (14), 144306.
(34) Shiomi, J. Nonequilirium molecular dynamics methods for lattice heat conduction calculations. *Annu. Rev. Heat Transfer* **2014**, *17*, 177.
(35) Stedman, G. E. Fermi's Golden Rule—An Exercise in Quantum Field Theory. *Am. J. Phys.* **1971**, *39* (2), 205−214.


https://dx.doi.org/10.1021/acs.nanolett.0c02983
*Nano Lett.* 2020, 20, 7513−7518

(36) Nitzan, A. *Chemical dynamics in condensed phases: relaxation, transfer and reactions in condensed molecular systems*, 1st ed.; Oxford University Press Inc.: New York, 2006.
(37) Cuevas, J. C.; Scheer, E. *Molecular electronics: an introduction to theory and experiment*, 2nd ed.; Reed, M., Ed.; World Scientific Series in Nanoscience and Nanotechnology; World Scientific Publishing Co. Pte. Ltd.: Singapore, 2017; Vol. 15.
(38) Xu, Y.; Wang, J.-S.; Duan, W.; Gu, B.-L.; Li, B. Nonequilibrium Green's function method for phonon-phonon interactions and ballistic-diffusive thermal transport. *Phys. Rev. B: Condens. Matter Mater. Phys.* **2008**, *78* (22), 224303.
(39) Wang, J.-S.; Agarwalla, B. K.; Li, H.; Thingna, J. Non-equilibrium Green's function method for quantum thermal transport. *Frontiers of Physics* **2014**, *9* (6), 673−697.
(40) Kong, L. T.; Bartels, G.; Campañá, C.; Denniston, C.; Müser, M. H. Implementation of Green's function molecular dynamics: An extension to LAMMPS. *Comput. Phys. Commun.* **2009**, *180* (6), 1004−1010.
(41) Plimpton, S. Fast Parallel Algorithms for Short-Range Molecular Dynamics. *J. Comput. Phys.* **1995**, *117* (1), 1−19.
(42) Harb, M.; Schmising, C. v. K.; Enquist, H.; Jurgilaitis, A.; Maximov, I.; Shvets, P. V.; Obraztsov, A. N.; Khakhulin, D.; Wulff, M.; Larsson, J. The c-axis thermal conductivity of graphite film of nanometer thickness measured by time resolved X-ray diffraction. *Appl. Phys. Lett.* **2012**, *101* (23), 233108.
(43) Stuart, S. J.; Tutein, A. B.; Harrison, J. A. A reactive potential for hydrocarbons with intermolecular interactions. *J. Chem. Phys.* **2000**, *112* (14), 6472−6486.
(44) Wang, Y.; Vallabhaneni, A. K.; Qiu, B.; Ruan, X. Two-Dimensional Thermal Transport in Graphene: A Review of Numerical Modeling Studies. *Nanoscale Microscale Thermophys. Eng.* **2014**, *18* (2), 155−182.
(45) Wang, L.; Li, B. Thermal Logic Gates: Computation with Phonons. *Phys. Rev. Lett.* **2007**, *99* (17), 177208.
(46) Ceriotti, M.; Bussi, G.; Parrinello, M. Nuclear Quantum Effects in Solids Using a Colored-Noise Thermostat. *Phys. Rev. Lett.* **2009**, *103* (3), No. 030603.
(47) Turney, J. E.; McGaughey, A. J. H.; Amon, C. H. Assessing the applicability of quantum corrections to classical thermal conductivity predictions. *Phys. Rev. B: Condens. Matter Mater. Phys.* **2009**, *79* (22), 224305.
(48) Bedoya-Martínez, O. N.; Barrat, J.-L.; Rodney, D. Computation of the thermal conductivity using methods based on classical and quantum molecular dynamics. *Phys. Rev. B: Condens. Matter Mater. Phys.* **2014**, *89* (1), No. 014303.
(49) Bo-Yu, Z.; Hui-Long, D.; Fei-Fan, C. Characterization of thermal conductivity for GNR based on nonequilibrium molecular dynamics simulation combined with quantum correction. *Acta Phys. Sin-Ch. Ed.* **2014**, *63* (7), No. 076501.
(50) Khan, A. I.; Navid, I. A.; Noshin, M.; Uddin, H. M. A.; Hossain, F. F.; Subrina, S. Equilibrium Molecular Dynamics (MD) Simulation Study of Thermal Conductivity of Graphene Nanoribbon: A Comparative Study on MD Potentials. *Electronics* **2015**, *4* (4), 1109.


https://dx.doi.org/10.1021/acs.nanolett.0c02983
*Nano Lett.* 2020, 20, 7513−7518